Chapter 4

Stable Charge Separation through Proton Displacements

4.0.1 ABSTRACT

As we have shown in the previous chapter, resolving the dynamic nuclear motion accompanying charge separation in bacterial reaction centers is crucial to understand how photosynthesis has optimized solar energy transduction. In this chapter we identify the pathway of primary electron transfer from the special pair excited state (P^*) to the accessory bacteriochlorophyll (B_A) using first-principles molecular dynamics and constrained density functional theory. We confirm that the oscillatory motion of a histidine at the interface between donor and acceptor initiates exciton dissociation and demonstrate how proton displacements are coupled to stable photoproduct formation.

Parts of this chapter were published in:
T. J. Eisenmayer, J. A. Lasave, A. Monti, H. J. M. de Groot, F. Buda, "Proton Displacements Coupled to Primary Electron Transfer in the Rhodobacter Sphaeroides Reaction Center", *Journal of Physical Chemistry B*, **2013**, 38, pp 11162-11168.
DOI: 10.1021/jp401195t

4.1 Introduction

In bacterial photosynthesis, sunlight is absorbed by antenna complexes that transfer the excitation energy to reaction centers where the photoinduced charge separation takes place [1]. The transition state of the primary photochemical reaction in the *Rhodobacter Sphaeroides* reaction center (bRC) is not reached through random thermal motion but through specific vibrational coherences that effectively modulate the barrier for charge separation [1,2] (see previous Chapter). This mechanism is of interest for artificial devices aiming for high-yield photon-to-charge conversion.

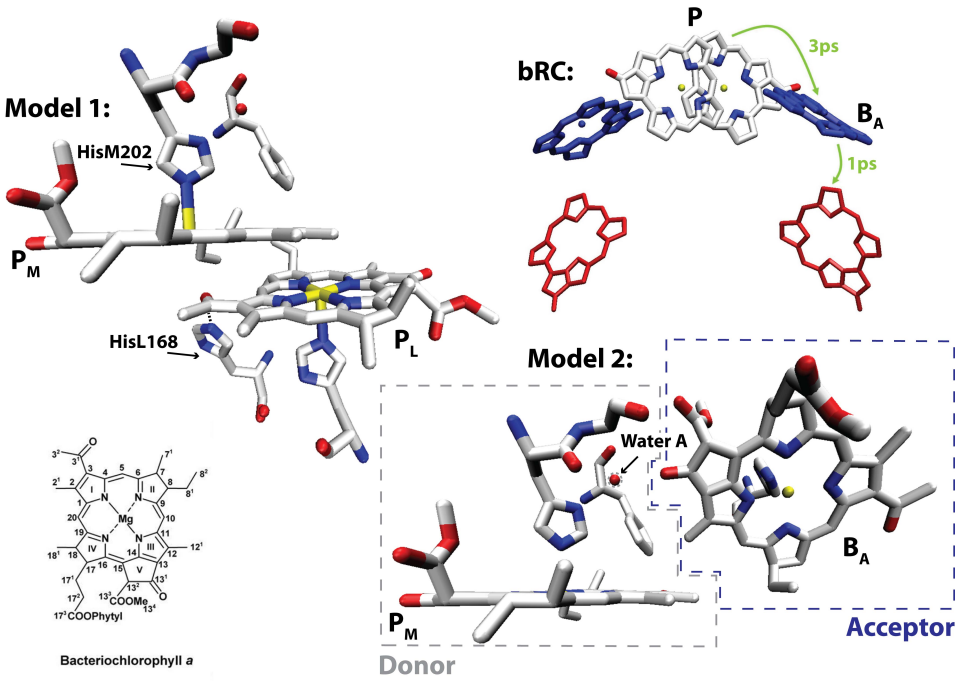

Figure 4.1: bRC (right top): Two-fold symmetric reaction center of *Rhodobacter sphaeroides* extracted from the latest 2.55 Å resolution X-ray structure (PDB entry 1M3X). The direction of electron transfer and corresponding time scales are denoted in green. Model **1** (left top): Including the special pair (P), axial histidines (HisL173 and HisM202), water A and B, and the diagonal symmetry-breaking residues PheM197 and HisL168. Model **2** (right bottom): Water A, the donor P_M, the primary acceptor B_A, the axial histidines (HisM202 and HisL153), and GlyM203. Inset (left bottom): Bacteriochlorophyll numbering.

The frequencies of these promoting vibrations are well-known from time-resolved spectroscopy [3-9]. In parallel, atomistic simulations are important because they can provide access to structural information that is inaccessible to spectroscopic methods. From the phenomenological study of Novoderezhkin and coworkers based on Redfield theory [2] we know that the formation of the first photoproduct is conveniently described by two vibrational coherences: a fast component of 100-150 cm^{-1} and a slower component of 30-35 cm^{-1}. The time scale of the primary photoinduced process in bRC is 3 ps, [10] and it occurs selectively along one of two pseudosymmetric cofactor branches (Figure 4.1) through a charge transfer (CT) intermediate [11,12] on the special pair (P). B_A is the accessory bacteriohlorophyll acting as primary acceptor. Subsequent electron transfer (ET) to form the secondary photoproduct along the A-branch, a reduced bacteriopheophytin (H_A^-), is very fast (1 ps). In this context, it is our aim to accurately characterize the reaction coordinate of the primary photoinduced charge separation from first principles. In previous work on the special pair, excited-state dynamics combined with a frequency analysis showed that a $\sim$100 cm^{-1} vibrational mode is coupled to the electronic excitation, leading to a CT intermediate ($P_L^+P_M^-$) [13]. Structurally, this $\sim$100 cm^{-1} mode involves a collective motion of P with most of the amplitude on P_M and the rotation of HisM202 as the characteristic coordinate. This is predicted to be the first/fast vibrational component that coherently modulates the charge transfer dynamics [2]. HisM202 is hydrogen bonded to an interstitial water (water A), which is held in place by a hydrogen-bond network connecting P_M and B_A. The loss of water A through site-directed mutation is accompanied by a slowing of the rate of ET by approximately a factor of 8 [14]. The second/slower vibrational component coupled to full charge separation is thus thought to involve the motion of water A with a frequency of $\sim$30-35 cm^{-1} [15]. The breaking of symmetry between cofactor chains is intimately related with the forward CT reactions. Although the special pair itself is already surrounded by the protein environment in a quasi-symmetric fashion (see Figure 4.1), on the L-side, HisL168 forms a hydrogen bond with the 3^1-acetyl of P_L, whereas on the M-side PheM197 does not. It is therefore plausible that even before excitation of P the ground-state electron density is asymmetrically distributed [16,17]. The vibrational mode corresponding to the hydrogen bond between P_L and HisL168 has been calculated to have a frequency of $\sim$50 cm^{-1}, and it is found to affect the stability of the cation ($P^{\bullet+}$) [13,18]. Here we employ atomistic simulations and single-point calculations to address (i) the role of the interstitial water A and (ii) the coupling of the ET process to configurational changes following the excitation and

(iii) upon oxidation of P.

4.2 Model and Methods

We extract the special pair (Model **1**) and the donor-acceptor model (Model **2**) from the latest X-ray crystallographic data of wild-type Rhodobacter sphaeroides at 2.55 Å resolution [19]. The special pair Model **1** includes the two Bacteriochlorophylls P_M and P_L, the five closest amino acids (GlyM203, PheM197, HisM202, HisL173, HisL168), and two interstitial waters (Figure 4.1). The donor-acceptor Model **2** includes P_M and its axially coordinated HisM202, taken as the donor of charge. B_A and its axially coordinated histidine HisL153 are taken as the charge acceptor (Figure 4.1). We also include PheM197 and GlyM203 to keep the whole protein pocket environment for the water A. For the entire system - Model **1** combined with Model **2** - we find that the HOMO and LUMO are localized on P_M and B_A, respectively, consistently with Model **2**. Moreover, the HOMO-LUMO gap is not significantly altered ($\sim$ 0.04 eV) and this justifies the exclusion of P_L from Model **2** to keep the system size minimal. The mechanical constraints induced by the protein environment are ensured by fixing the tails of the histidines, the phenylene, and the glycine. Because of their length the phytyl side chains are sterically hindered within the protein and are known not to affect the electronic structure of the bacteriochlorophylls [17]. Hence they are reduced to a methyl group that is fixed. The AIMD simulations have been performed using the Car-Parrinello method [20,21] as implemented in the CPMD code [22] with a time step of 0.1 fs. A Nosé thermostat is used in all simulations to keep the temperature around an average of 300 K. The time scales of the simulation runs for Model **1** were kept $\sim$ 1 ps for ground, excited, and radical cation states. For Model **2** a ground-state simulation is performed for $\sim$ 2 ps. It should be stressed that this simulation is not aimed at the explicit description of the nonadiabatic ET from P^* to B_A^- in real-time, which would require modeling the evolution of the excited electronic state (see Chapter 6) on a time scale of $\sim$ 3 ps. The main goal of this AIMD simulation is to investigate the stability of the interstitial water and the thermal fluctuations in the hydrogen-bonding network established between the donor and acceptor. Both models are stable along the dynamics with a root-mean-square displacement (RMSD) that fluctuates around an average value of 0.8 Å for Model **2**, slightly larger than the RMSD of Model **1** (0.6 Å). The BLYP functional [24,25] is used for the exchange-correlation energy, which is known to yield hydrogen bonds that are in good agreement with experiment. The Kohn-Sham orbitals are ex-

panded in a plane-wave basis set with an energy cutoff of 70 Ry. We employ dispersion-corrected atom-centered (DCACP) pseudopotentials [26,27]. To study the frequency domain, we perform Fourier transforms of the velocity autocorrelation function of the AIMD trajectory. We can in this way obtain specific characteristic frequencies of individual structural parameters (i.e., bond distances, bond angles). The recently developed computational method of Constrained Density Functional Theory (CDFT) is used to verify the predicted reaction coordinate of primary charge separation. This method was specifically developed by Wu and van Voorhis [21] to address long-range CT states. It has been shown that CDFT can accurately describe the excitation energy and its dependence on the donor-acceptor distance [28]. The CDFT calculations are performed with the same functional, basis set, and pseudopotentials used for the AIMD simulations. In the CDFT method applied to bRC, the charge-localized states (or diabatic states) A and B are obtained from two DFT calculations. The first represents the initial state where no ET between donor and acceptor has occurred yet (state A), while the second (state B) describes the charge-separated state obtained by constraining a positive charge on the donor and a negative charge on the acceptor. The resulting ground-state density $\rho(r)$ on each diabatic state will satisfy the constraint

$$\int_V W(r)\rho(r)dr = N_c \tag{4.1}$$

where $W(r)$ is the operator that defines the electronic population and the integral runs over the entire volume of the system. N_c is the value of the constraint defined as the charge difference between the net charge on the donor and acceptor group: $N_c = N_{don} - N_{acc}$. Therefore, we choose $N_c = 0$ for state A and $N_c = 2$ for state B. For the population operator we use the Hirshfeld partitioning scheme [29] as implemented in the CPMD code [30].

4.3 Results

AIMD Simulations

Previous AIMD simulations on the special pair (Model **1**) ground and excited state found two important degrees of freedom coupled to electronic structure rearrangements of P: (1) the rotation of HisM202 with respect to the Mg-N_τ coordination axis and (2) the hydrogen bond between P_L and HisL168 [13]. Here we extend these simulations to analyze the oxidized radical cation state. The first degree of freedom and characteristic coordinate of the

vibrational mode coupled to the formation of the CT intermediate involves the rotation of the axial histidine M202. From Figure 4.2(a), which shows the compiled trajectories for ground state, excited state, and radical cation, it can be seen that HisM202 rotates upon excitation to an average dihedral angle of 80° with respect to the Mg-N_τ coordination axis. Upon oxidation this conformational rearrangement is reversed and the dihedral angle rotates back to the ground-state values.

Figure 4.2: AIMD simulations in P, P^* and $P^{\bullet+}$.

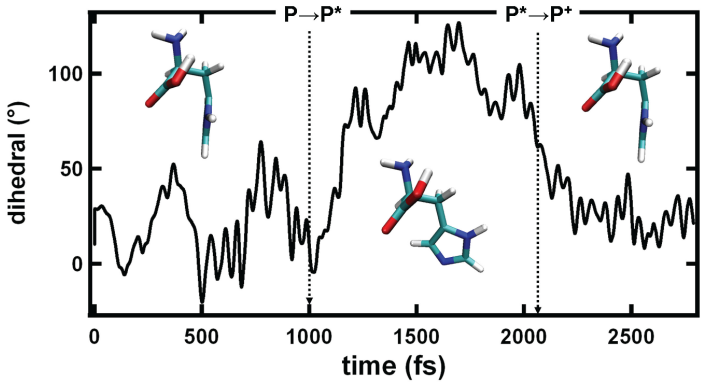

(a) AIMD simulations of Model **1** showing the time evolution of the HisM202 dihedral angle with respect to the Mg-N_τ coordination axis along the ground (0 to 1.0 ps), excited (1.0 to 2.1 ps), and oxidized state (2.1 to 2.8 ps) trajectories.

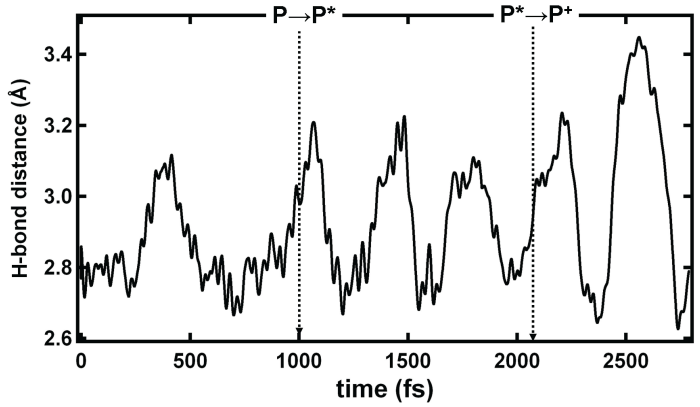

(b) N···O hydrogen-bond distance between HisL168 and the 3^1-acetyl of P_L for ground state (0 to 1.0 ps), excited state (1.0 to 2.1 ps), and radical cation (2.1 to 2.8 ps) AIMD trajectories. Upon excitation no changes in the amplitude of the fluctuations are observed, whereas in the radical cation state the hydrogen bond is weakened, representing a proton displacement.

Inversely, the second important degree of freedom involving the hydrogen bond between the 3^1-acetyl of P_L and HisL168 (see Figure 4.1) shows no significant changes going from ground to excited state. However, upon oxidation the oscillations become larger and the hydrogen bond is on average weakened (Figure 4.2(b)).

For the donor-acceptor model (Model 2) a room-temperature AIMD simulation is performed extending over 2 ps. DFT single-point calculations performed at several snapshots along the trajectory show consistently that the HOMO is localized on P_M and the LUMO is localized on B_A. The LUMO electron density extends over the interstitial water A, whereas the HOMO shows no electron density in this region, although it does extend over the axial histidine M202. To understand the structural cause of HOMO-LUMO localization we investigated the planarity of both chromophores taking into account the C_3-C_7-C_{12}-C_{17} dihedral angle (see inset, Figure 4.1). P_M is found to be the more distorted chromophore, whereas B_A is almost perfectly planar. Another factor influencing the HOMO-LUMO localization is the orientation of the axial histidines relative to the Mg-N_τ axis. For P_M the dihedral angle of the axially coordinated histidine, averaged over the dynamics, is 21°, whereas for B_A this angle is -108°. The position of water A in its hydrogen-bond network is stable throughout the dynamics. The average position of water A is halfway between the HisM202-nitrogen and the 13^1-keto-carbonyl of B_A.

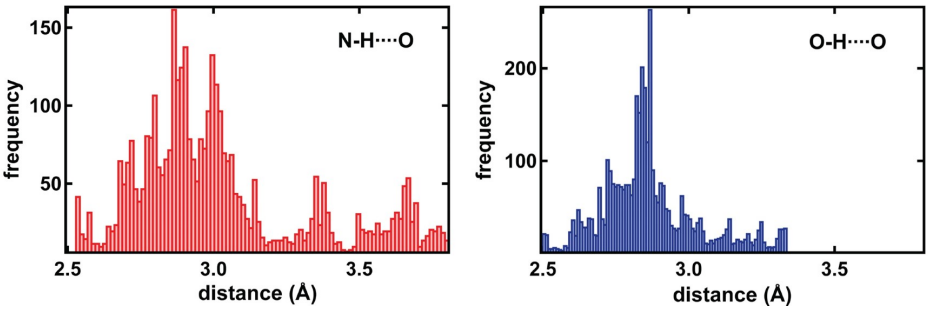

Figure 4.3: Distribution of distances centered around the interstitial water A oxygen atom sampled during the AIMD simulations of Model 2 in the ground state. Left graph (red) distribution of N-H···O distances representing the hydrogen bond with HisM202. Right graph (blue) distribution of O-H···O distances representing the hydrogen bond with the keto carbonyl of B_A.

Figure 4.3 shows the distribution of N-H···O and O-H···O distances. The most frequently occurring separation is ∼2.8 Å for both degrees of freedom. The N-H···O distances additionally have a tail at larger separations with peaks at 3.4 and 3.7 Å. Dynamically, both protons of water A form and break hydrogen bonds with the keto carbonyl of B_A in a "switching" motion (Figure 4.4(a,b)). A Fourier analysis of this motion, in terms of hydrogen-bond angles and distances, gives a frequency of 30-35 cm^{-1} for the breaking and forming of the keto carbonyl hydrogen bonds (Figure 4.4(c)). The weakest hydrogen bond of water A is with GlyM203, which is rarely formed during the 2 ps ground-state trajectory.

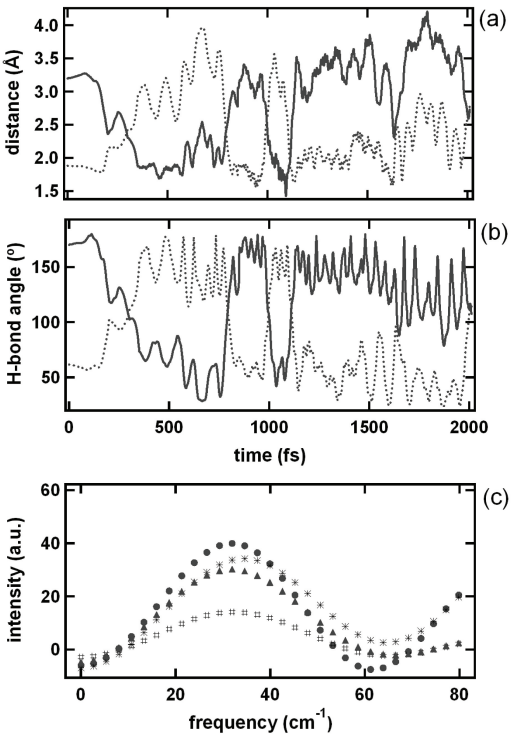

Figure 4.4: Hydrogen bond H···O distance (a) and O-H···O angle (b) along the dynamical trajectory. The full and dotted line show the two protons of water A that break and form hydrogen bonds in a "switching" motion with the keto 13^1 carbonyl group of B_A. The bottom graph (c) shows the Fourier transform of this molecular motion between water A and the keto carbonyl group of B_A with a first peak at 30-35 cm^{-1} in agreement with the experimental result of Yakovlev et al. [15].

Constrained DFT

To explore the reaction coordinate of excited-state relaxation and ET we performed CDFT calculations constraining a positive charge on the donor (P_M) and a negative charge on the acceptor (B_A). Following the HOMO-LUMO analysis, we include the axial histidine HisM202 in the donor and the axial histidine HisL153 in the acceptor. Energies are calculated as a function of the dihedral angle corresponding to the HisM202 rotation (see Figure 4.2(a)). For each value of the dihedral angle we optimize the other degrees of freedom including the position of water A. The energy difference between the ground state and the vertical charge separated state - calculated with CDFT at the ground state geometry - decreases along the suggested reaction coordinate, as shown in Figure 4.5.

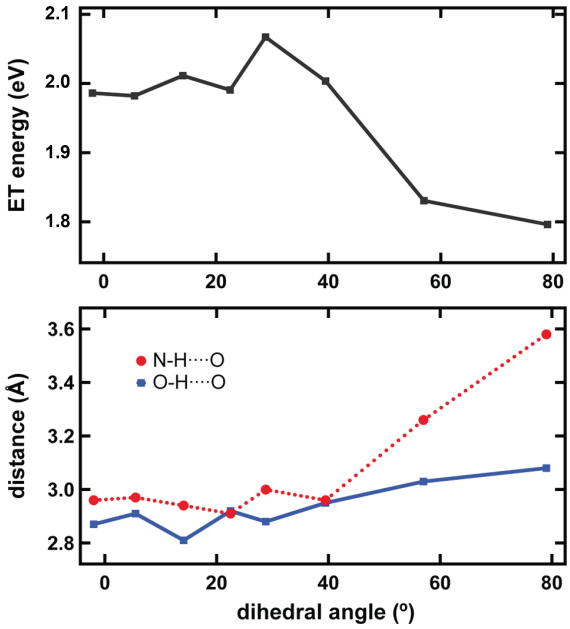

Figure 4.5: Top: Vertical electron transfer (ET) energy dependence on the dihedral angle of HisM202 with respect to the Mg-N_τ coordination axis. Bottom: N-H$\cdots$O (circles) and O-H$\cdots$O (squares) hydrogen-bond distances as a function of the same dihedral angle.

The results in Figure 4.5 show that the vertical ET energy decreases along the collective reaction coordinate approximated by the rotation of HisM202. We also observe that along this coordinate proton displacement

accompany the charge separation: The rotation of HisM202 displaces water A in its hydrogen-bond pocket toward the carbonyl of B_A and GlyM203 (Figure 4.5). After ET the N-H$\cdots$O distance increases to 3.6 Å, representing a considerable weakening of the hydrogen bond between the water and HisM202 (Figure 4.5). Interestingly, it is apparent that already in the ground state this conformation of the hydrogen-bond network is occasionally sampled (see Figure 4.3). Thus, while our results show no direct evidence for full proton coupled electron transfer (PCET) they indicate proton displacements coupled to the reaction coordinate.

Finally, within the entire model it is possible to verify that the unoccupied Kohn-Sham states on the special pair are higher in energy than the unoccupied Kohn-Sham state on B_A. Indeed, the lowest LUMO on P^* is 0.14 eV higher in energy than the LUMO on B_A (Figure 4.6). This represents a small overestimation with respect to experiment, where the negative energy gradient (ΔG) is estimated to be $\sim$ -0.06 eV [34].

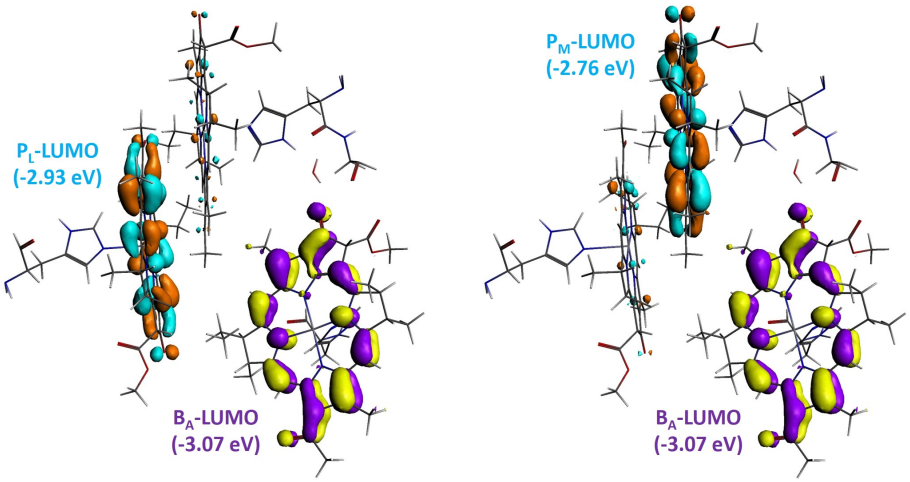

Figure 4.6: Left: Spatial distribution and energies of the LUMO on P_L and on B_A. Right: Spatial distribution and energies of the LUMO on P_M and on B_A. As detailed in Chapter 3, the frontier orbitals on the special pair exhibit dynamic localization and the initial excitonic state can thus involve a population of either $P_L \cdot LUMO$ or $P_M \cdot LUMO$. The orbitals calculated at the B3LYP/TZP level of theory and their associated dynamics (Chapter 3) reveal that there is a reaction coordinate for photoinduced charge separation to the $B_A \cdot LUMO$.

4.4 Discussion and Conclusions

In this chapter, we elucidate the conformational rearrangements that couple to the full ET from the special pair excited state of bRC to the primary acceptor B_A. The charge separation is highly optimized and known to occur at an optimal rate [33]. Recently, this rate was found to be governed by a single (Goldilocks) parameter Λ that at the point of optimum transfer is equal to $1/\sqrt{2}$ [35].

$$\Lambda_{opt} = \frac{\lambda T}{\gamma_c \Delta G} = \frac{1}{\sqrt{2}} \tag{4.2}$$

If we consider the ambient conditions at which bRC operates ($300K \sim 26meV$), the experimental value for the reorganization energy ($\lambda \sim 28meV$ [36]) and for the energy gradient ($\Delta G \sim 65meV$ [34]), the only unknown parameter remains the bath correlation time γ_c. As this parameter describes the correlation between the electronic states (P^*B and PB^-) and the (protein) environment, we provide the value of the first low frequency mode that couples to ET ($100cm^{-1} \sim 12.5meV$). Then, indeed the Goldilocks parameter is $\sim 1/\sqrt{2}$.

In Chapter 3, the coordinate of this low frequency mode was found to involve the rotation of HisM202, which from Figure 4.2a is seen to be reversible upon oxidation. This rotation displaces the protons of water A toward GlyM203 and the 13^1-carbonyl of B_A in a collinear fashion with respect to the direction of ET (Figure 4.7). The proton displacement is found to have a frequency of 30-35 cm^{-1} in good agreement with experiment and thus gives a structural interpretation to the second coordinate of charge separation suggested in the phenomenological study by Novoderezhkin and coworkers [2]. In contrast with Ivashin and Larsson, who propose a double proton-transfer mechanism within the hydrogen-bond network surrounding water A [37], we observe proton displacements following ET (Figures 4.5 and 4.7). In the ground state, these conformations are already occasionally sampled (Figure 4.3), although the average distance of water A from HisM202 is 2.9 Å. In the charge-separated state we find a new equilibrium value of 3.6 Å at the same approximate values where the ground-state histogram exhibits a long tail (Figure 4.3). The second proton displacement found to couple to oxidation of P involves the weakening of the hydrogen bond between HisL168 and the 3^1-acetyl of P_L. The weakening of this interaction destabilizes the HOMO of P_L [13], the site on which most of the positive charge is localized in $P^{\bullet+}$ [38], and therefore

reduces the driving force for charge recombination. Experimental evidence for such a mechanism is possibly given by Deshmukh and coworkers [39], who find a light-induced hypsochromic shift in *Rhodobacter capsulatus* and suggest this to be caused by the 3^1-acetyl group.

In conclusion, the reaction coordinate of initial charge separation in the *Rhodobacter sphaeroides* reaction center is a multidimensional landscape. First, upon excitation a reversible conformational rearrangement stabilizes the charge transfer from P_L to P_M, mostly involving the rotation of HisM202 with a characteristic frequency of $\sim$ 100 cm^{-1}. Second, through this rotation a proton is displaced in the hydrogen network surrounding water A with a frequency of 30-35 cm^{-1}. Finally, on a longer time scale, another proton is displaced from the 3^1-acetyl of P_L toward HisL168, which destabilizes the cation $P^{\bullet+}$ by mixing in the $P^{\bullet}$ neutral radical state. This effectively reduces the driving force for charge recombination. Together these rearrangements present a structural framework for understanding the highly efficient and coherent CT process from the special pair excited state to the primary charge-separated state.

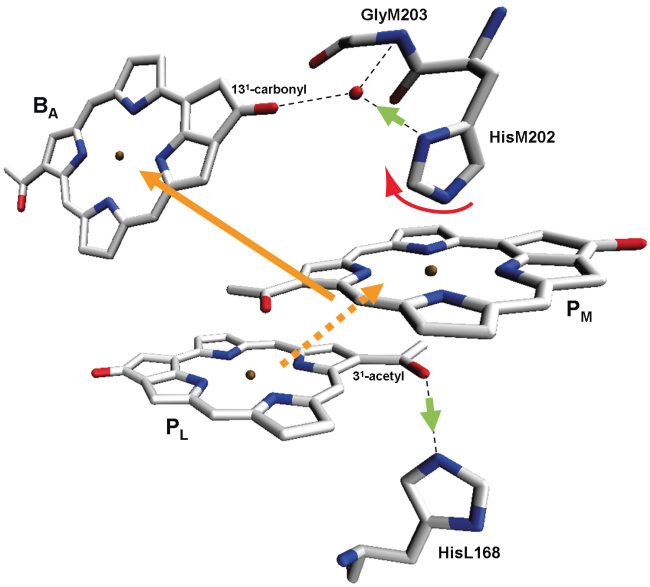

Figure 4.7: Schematic representation of the nuclear motion (green and red arrows) accompanying the charge and electron transfer processes (orange arrows).

4.5 References

[1] Deisenhofer, J.; Epp, O.; Miki, K.; Huber, R.; Michel, H. Structure of the Protein Subunits in the Photosynthetic Reaction Centre of Rhodopseudomonas Viridis at 3Å Resolution. *Nature* **1985**, 318, 618-624.

[2] Novoderezhkin, V.; Yakovlev, A.; van Grondelle, R.; Shuvalov, V. Coherent Nuclear and Electronic Dynamics in Primary Charge Separation in Photosynthetic Reaction Centers: A Redfield Theory Approach. *J. Phys. Chem. B* **2004**, 108, 7445-7457.

[3] Vos, M. H.; Jones, M. R.; Hunter, C. N.; Breton, J.; Martin, J. L. Coherent Nuclear Dynamics at Room Temperature in Bacterial Reaction Centers. *Proc. Natl. Acad. Sci. U.S.A.* **1994**, 91, 12701-12705.

[4] Vos, M. H.; Jones, M. R.; Martin, J. L. Vibrational Coherence in Bacterial Reaction Centers: Spectroscopic Characterisation of Motions Active during Primary Electron Transfer. *Chem. Phys.* **1998**, 233, 179-190.

[5] Rischel, C.; Spiedel, D.; Ridge, J. P.; Jones, M. R.; Breton, J.; Lambry, J. C.; Martin, J. L. Low Frequency Vibrational Modes in Proteins: Changes Induced by Point-Mutations in the Protein- Cofactor Matrix of Bacterial Reaction Centers. *Proc. Natl. Acad. Sci. USA.* **1998**, 95, 12306-12311.

[6] Reddy, N. R.; Kolaczkowski, S. V.; Small, G. J. A Photoinduced Persistent Structural Transformation of the Special Pair of a Bacterial Reaction Center. *Science* **1993**, 260, 68-71.

[7] Cherepy, N. J.; Shreve, A. P.; Moore, L. J.; Franzen, S.; Boxer, S. G.; Mathies, R. a. Near-Infrared Resonance Raman Spectroscopy of the Special Pair and the Accessory Bacteriochlorophylls in Photosynthetic Reaction Centers. *J. Phys. Chem.* **1994**, 98, 6023-6029.

[8] Yakovlev, A. G.; Shkuropatov, A. Y.; Shuvalov, V. A. Nuclear Wave Packet Motion between $P*$ and $P^{+}B_{A}^{-}$ Potential Surfaces with a Subsequent Electron Transfer to HA in Bacterial Reaction Centers at 90 K. Electron Transfer Pathway. *Biochemistry* **2002**, 41, 14019-14027.

[9] Shuvalov, V.; Yakovlev, A. Coupling of Nuclear Wavepacket Motion and Charge Separation in Bacterial Reaction Centers. *FEBS Lett.* **2003**, 540, 26-34.

[10] Moore, L. J.; Zhou, H.; Boxer, S. G. Excited-State Electronic Asymmetry of the Special Pair in Photosynthetic Reaction Center Mutants: Absorption and Stark Spectroscopy. *Biochemistry* **1999**, 38, 11949-11960.

[11] Cohen Stuart, T.; van Grondelle, R. Multipulse Spectroscopy on the Wild-Type and YM210W Bacterial Reaction Centre Uncovers a New Intermediate State in the Special Pair Excited State. *Chem. Phys. Lett.* **2009**, 474, 352-356.

[12] Holzapfel, W.; Finkele, U.; Kaiser, W.; Oesterhelt, D.; Scheer, H.; Stilz, H. U.; Zinth, W. Initial Electron-Transfer in the Reaction Center from Rhodobacter

Sphaeroides. *Proc. Natl. Acad. Sci. U.S.A.* **1990**, 87, 5168-5172.

[13] Eisenmayer, T. J.; de Groot, H. J. M.; van de Wetering, E.; Neugebauer, J.; Buda, F. Mechanism and Reaction Coordinate of Directional Charge Separation in Bacterial Reaction Centers. *J. Phys. Chem. Lett.* **2012**, 3, 694-697.

[14] Potter, J. A.; Fyfe, P. K.; Frolov, D.; Wakeham, M. C.; Grondelle, R. V.; Robert, B.; Jones, M. R. Strong Effects of an Individual Water Molecule on the Rate of Light-driven Charge Separation in the Rhodobacter sphaeroides Reaction Center. *Biochemistry* **2005**, 280, 27155-27164.

[15] Yakovlev, A. G.; Shuvalov, V. A. Electron Transfer in Deuterated Reaction Centers of Rhodobacter Sphaeroides at 90 K According to Femtosecond Spectroscopy Data. *Biochemistry* **2003**, 68, 603-610.

[16] Daviso, E.; Prakash, S.; Alia, A.; Gast, P.; Neugebauer, J.; Jeschke, G.; Matysik, J. The Electronic Structure of the Primary Electron Donor of Reaction Centers of Purple Bacteria at Atomic Resolution as Observed by Photo-CIDNP 13C NMR. *Proc. Natl. Acad. Sci. U.S.A.* **2009**, 106, 22281-22286.

[17] Wawrzyniak, P. K.; Beerepoot, M. T. P.; de Groot, H. J. M.; Buda, F. Acetyl Group Orientation Modulates the Electronic Ground-State Asymmetry of the Special Pair in Purple Bacterial Reaction Centers. *Phys. Chem. Chem. Phys.* **2011**, 13, 10270-10279.

[18] Rautter, J.; Lendzian, F.; Schulz, C.; Fetsch, A.; Kuhn, M.; Lin, X.; Lubitz, W. ENDOR Studies of the Primary Donor Cation Radical in Mutant Reaction Centers of Rhodobacter Sphaeroides with Altered Hydrogen-Bond Interactions. *Biochemistry* **1995**, 34, 8130-8143.

[19] Camara-Artigas; Brune, D.; Allen, J. P. Interactions between Lipids and Bacterial Reaction Centers Determined by Protein Crystallography. *Proc. Natl. Acad. Sci. U.S.A.* **2002**, 99, 11055-11060.

[20] Car, R.; Parrinello, M. Unified Approach for Molecular Dynamics and Density-Functional Theory. *Phys. Rev. Lett.* **1985**, 55, 2471.

[21] Marx, D.; Hutter, J. Ab Initio Molecular Dynamics: Basic Theory and Advanced Methods; Cambridge University Press: Cambridge, U.K., **2009**.

[22] Wu, Q.; Van Voorhis, T. Constrained Density Functional Theory and its Application in Long-Range Electron Transfer. *J. Chem. Theory Comput.* **2006**, 2, 765-774.

[23] CPMD v3.11.1, Copyright IBM Corp, 1990-2008; Copyright MPI fuür Festkörperforschung Stuttgart, 1997-2001. http://www.cpmd.org/.

[24] Becke, A. D. Density-Functional Exchange-Energy Approximation with Correct Asymptotic Behavior. *Phys. Rev. A* **1988**, 38, 3096.

[25] Lee, C.; Yang, W.; Parr, R. G. Development of the Colle-Salvetti Correlation-energy Formula into a Functional of the Electron Density. *Phys. Rev. B* **1988**, 37, 785.

[26] von Lilienfeld, O. A.; Tavernelli, I.; Rothlisberger, U.; Sebastiani, D. Optimization of Effective Atom Centered Potentials for London Dispersion Forces in Density Functional Theory. *Phys. Rev. Lett.* **2004**, 93, 153004.

[27] von Lilienfeld, O. A.; Tavernelli, I.; Rothlisberger, U.; Sebastiani, D. Performance of Optimized Atom-centered Potentials for Weakly Bonded Systems Using Density Functional Theory. *Phys. Rev. B* **2005**, 71, 195119.

[28] Wu, Q.; Van Voorhis, T. Direct Optimization Method to Study Constrained Systems Within Density-functional Theory. Phys. Rev. A 2005, 72, 024502.

[29] Hirshfeld, F. L. Bonded-atom Fragments for Describing Molecular Charge Densities. *Theor. Chem. Acc.* **1977**, 44, 129.

[30] Oberhofer, H.; Blumberger, J. Electronic Coupling Matrix Elements From Charge Constrained Density Functional Theory Calculations Using a Plane Wave Basis Set. *J. Chem. Phys.* **2010**, 133, 244105.

[31] Marcus, A.; Sutin, N. Electron Transfers in Chemistry and Biology. *Biochim. Biophys. Acta* **1985**, 811, 265.

[32] Moser, C. C.; Keske, J. M.; Warncke, K.; Farid, R. S.; Dutton, L.P. Nature of Biological Electron Transfer. *Nature* **1992**, 355, 796-802.

[33] Blumberger, J. Free Energies for Biological Electron Transfer from QM/MM Calculation: Method, Application and Critical Assessment. *Phys. Chem. Chem. Phys.* **2008**, 10, 5651-5667.

[34] Smith, D. M. A.; Rosso, K. M.; Dupuis, M.; Valiev, M.; Straatsma, T. P. Electronic Coupling between Heme Electron-Transfer Centers and Its Decay with Distance Depends Strongly on Relative Orientation. *J. Phys. Chem. B* **2006**, 110, 15582-15588.

[35] L. Mourokh and S. Lloyd, Optimal rates for electron transfer in Marcus theory, *Phys. Rev. E.*, **2013**, 88, 42819.

[36] D. C. Arnett, C. Moser, P. L. Dutton and N. F. Scherer, The First Events in Photosynthesis: Electronic Coupling and Energy Transfer Dynamics in the Photosynthetic Reaction Center from Rhodobacter sphaeroides, *J. Phys. Chem. B*, **1999**, 103, 2014-2032.

[37] Ivashin, N.; Larsson, S. Trapped Water Molecule in the Charge Separation of a Bacterial Reaction Center. *J. Phys. Chem. B* **2008**, 112, 12124.

[38] Lendzian, F.; Huber, M.; Isaacson, R. A.; Endeward, B.; Plato, M.; BoÌĹnigk, B.; MoÌĹbius, K.; Lubitz, W.; Feher, G. The Electronic Structure of the Primary Donor Cation Radical in Rhodobacter Sphaeroides R-26: ENDOR and TRIPLE Resonance Studies in Single Crystals of Reaction Centers. *Biochim. Biophys. Acta* **1993**, 1183, 139-160.

[39] Deshmukh, S. S.; Akhavein, H.; Williams, J. C.; Allen, J. P.; KaÌĄlmaÌĄn, L. Light-Induced Conformational Changes in Photosynthetic Reaction Centers: Impact of Detergents and Lipids on the Electronic Structure of the Primary Electron Donor. *Biochemistry* **2011**, 50, 5249-5262.

"I must Create a System, or be enslav'd by another Man's.
I will not Reason and Compare;
my business is to Create."

— William Blake —
Jerusalem (1804)